Sheath structure in a magnetized plasma

D. L. Holland,[a] B. D. Fried, and G. J. Morales
Department of Physics, University of California, Los Angeles, Los Angeles, California 90024-1547

(Received 28 September 1992; accepted 24 February 1993)

The sheath formed between a magnetized plasma and a particle absorbing wall is examined for the case in which the magnetic field intercepts the wall at a small angle $0° < \epsilon \lesssim 9°$, where $\sin\epsilon = \mathbf{B}\cdot\hat{n}/|B|$, and $\hat{n}$ is the unit normal to the wall. The model is time-independent and one-dimensional (1-D) with all functions varying only in the direction normal to the wall. The ions are modeled by a Maxwellian velocity distribution which is modified by the condition that ions, which would have hit the wall, are absent. For the electrons a fluid description is used, including the effects of electron–neutral collisions. The transport of particles due to turbulent electrostatic fluctuations is modeled by a constant electric field perpendicular to both $\mathbf{B}$ and $\hat{n}$. It is found that in the range of angles under consideration, there are two distinct regimes of sheath formation. If $\epsilon \lesssim \bar{\nu} = \nu/\Omega_e$ (grazing incidence), where ν is the electron–neutral collision frequency and Ω_e is the electron cyclotron frequency, then the properties of the sheath are determined by a parameter λ which is the ratio of the convective ($\mathbf{E}\times\mathbf{B}$) and diffusive electron flows. If $\lambda \lesssim 1$, the wall potential is negative and the sheath scale length is on the order of an ion gyroradius. If $\lambda \gtrsim 1$, the wall potential is positive and, for large λ, the sheath is characterized by two scales: a short length, which is a decreasing function of λ, adjacent to the wall, and the ion gyroradius farther from the wall. For $\epsilon \gg \bar{\nu}$, (oblique incidence) the potential at the wall is negative with a magnitude close to that of the unmagnetized plasma and is only weakly dependent on ϵ. In addition, for this case, the sheath scale length is on the order of an ion gyroradius and is weakly dependent on ϵ, larger values of ϵ resulting in a slightly shorter scale length.

I. INTRODUCTION

In recent years, the sheath formed between a magnetized plasma and a particle absorbing wall has received a considerable amount of attention. A primary motivation has been an increasing recognition of the importance of the edge region for the overall confinement properties of magnetized plasmas. In addition, the sheath has a significant influence on the particle and energy flux to the wall, which in turn can modify such characteristics as wall sputtering and other sources of impurities. Theoretical efforts in this area have analyzed two separate and distinct regimes: (1) a magnetic field perfectly parallel to the wall, where the angle of incidence $\epsilon = 0$, and (2) a magnetic field obliquely incident on the wall, typically $\epsilon \gtrsim 1°$, where $\sin\epsilon = (\mathbf{B}\cdot\hat{\mathbf{n}})/|B|$, $\hat{\mathbf{n}}$ being the unit normal to the surface. In the first case, which has been examined analytically by Daybelge and Bein[1] and, with the aid of particle codes, by Theilhaber and Birdsall[2,3] and Gerver *et al.*,[4] the finite ion cyclotron radius results in a preferential loss of ions from the plasma, so the potential at the wall is positive with respect to the plasma interior. In the second case, which has been studied by Chodura[5] using a particle-in-cell code, electrons can leave the plasma along the field line faster than the ions can cross the field, so the potential at the wall is negative with respect to the interior. At some small but finite value of ϵ, the wall potential should change from negative to positive.

In this paper, we analyze the magnetized sheath over a range of angles of incidence, $0 \leqslant \epsilon \leqslant 9°$, using a very simple one-dimensional (1-D) (functions vary only in the direction normal to the wall), time-independent (no waves or fluctuations) plasma model. The ions are assumed to have a Maxwellian velocity distribution perpendicular to $\mathbf{B}$, but ions which would have been intercepted by the wall are removed from the distribution function. The electrons are described by the warm fluid equations with electron–neutral collisions included. The loss of particles to the wall due to the turbulent electric fields ubiquitously present in confined plasmas is modeled by the imposition of an "effective" constant electric field normal to both $\mathbf{B}$ and $\hat{\mathbf{n}}$. A complete discussion of the use of a constant effective electric field to model turbulent $\mathbf{E}\times\mathbf{B}$ transport may be found in Ref. 6, however, in essence it assumes that the fluctuating electric field is electrostatic in nature and that the density and potential fluctuations are related through a linearized Boltzmann relation. If, in addition, we assume that the fluctuation spectrum is sharply peaked in frequency so that we may use a monochromatic spectrum, the effective electric field may be approximated as $E_y = (2T_e/q)\ k_y \times |q\delta\phi/T_e|^2$, where $\delta\phi$ and k_y are the amplitude and inverse wavelength of the potential fluctuations, respectively, and T_e is the electron temperature. This model of particle transport due to turbulent electric fields is separate from the stochastic transport across a magnetized sheath due to the interaction of small amplitude waves and large-scale vorticies, as discussed by Parker *et al.*[7] and as seen in the self-consistent simulations of Thielhaber and Birdsall.[2,3] We assume that the plasma parameters are such that the Debye length, L_D, and the cyclotron radii satisfy

[a]Present address: Naval Research Laboratory, code 6792, Washington, D.C. 20375-5346.

 0899-8221/93/061723-15$06.00 © 1993 American Institute of Physics

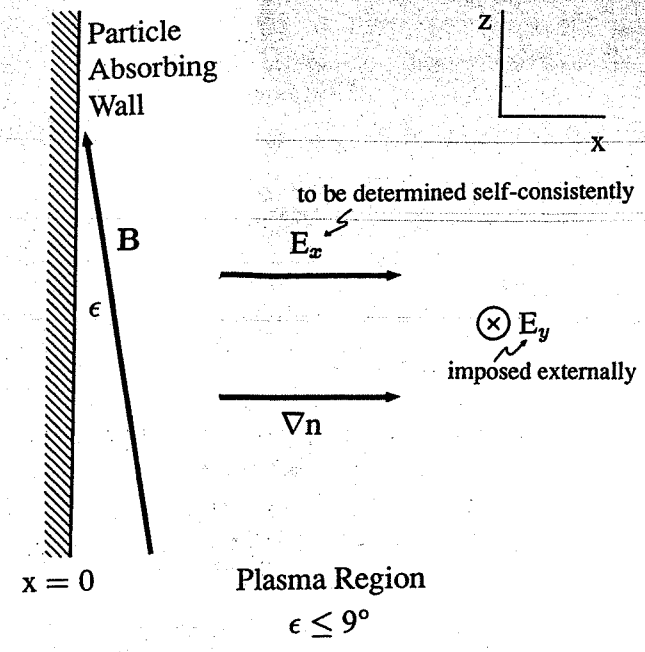

FIG. 1. Geometry of the fields used in the sheath calculation.

$r_{ci} \gg L_D \gg r_{ce}$. (This is generally the case in tokamak edge plasmas for instance.)

Of course, this simple model neglects a host of physical effects likely to be present in many sheaths, such as sputtering, impurities, ionization, recombination, etc. If these are included, the problem can only be attacked with computer simulations, and while these can give numerical results for specific configurations, it is difficult to determine parametric dependences and scaling laws. (An interesting review of the state of the art in particle simulations, including many of the effects listed above, has recently been written by Birdsall.[8]) Our objective is to characterize, in as general a form as possible and in terms of appropriate dimensionless variables, the intrinsic properties of a magnetized sheath. (Our results are, for the most part in closed form, although some numerical work is necessary, e.g., in evaluating complicated analytic expressions or solving Poisson's equation.) With these results in hand, the consequences of incorporating the various additional physical phenomena mentioned above can then be studied.

As illustrated in Fig. 1, we use slab geometry, in which x corresponds to the radial direction in toroidal geometry while y and z correspond to the poloidal and toroidal directions, respectively. All variables are functions of x alone. If the potential $\Phi(x)$ is known, it is, in principle, a straightforward matter to find the ion orbits and thus determine, for each point in the $(x,\mathbf{v})$ phase space, whether an ion located there would have hit the wall at some previous time. Removing such "inadmissible" ions from the assumed Maxwellian distribution function we would then integrate over $\mathbf{v}$ to find the ion density $n_i(x)$. To actually determine the admissibility of each point in the ion phase space, however, would require extensive orbit calculations, even if $\Phi(x)$ were known. Since $\Phi(x)$ is to be determined self-consistently, using Poisson's equation, this leads to a sizable computer simulation problem. We avoid that by finding an effective potential for the motion along x and using energy arguments to obtain a simple, approximate criterion for admissibility. (This procedure assumes that the effective potential has a single minimum within the sheath, a condition which is found, *a posteriori*, to be satisfied for most cases of interest.) The admissible ions are those which are trapped in the effective potential well and they lie within a parabola in the v_x, v_y plane.

For the electrons, the warm fluid equations give a first order differential equation for the electron density $n_e(x)$ in terms of the potential $\Phi(x)$. Solving this for n_e and then substituting n_e and n_i into Poisson's equation (with suitable boundary conditions) would yield an integrodifferential equation for the self-consistent potential Φ. Instead of solving that equation, it proves more convenient to express n_e in terms of Φ and $n_i(\Phi)$ using Poisson's equation, and then substitute this into the differential equation for n_e, obtaining a third-order differential equation for Φ.

Our results are expressed in terms of a few dimensionless parameters. Four are conventional: the temperature ratio, $\theta \equiv T_e/T_i$; the ratio of electron–neutral collision frequency to electron cyclotron frequency, $\bar{\nu} \equiv \nu/\Omega_e$; the ratio of the outward E_y drift velocity to the ion thermal velocity, $u_E \equiv c|E_y|/B_0 v_{ti}$; and the ratio of ion cyclotron radius to electron Debye length, $\alpha \equiv r_{ci}/L_D$. An additional, very important parameter, $\lambda \equiv 2u_E\bar{\nu}/\theta(\bar{\nu}^2+\epsilon^2)$, measures the relative importance of the two mechanisms for electron loss, namely cross-field convection (fluctuation-induced $\mathbf{E}\times\mathbf{B}$ drift) and diffusion across (or, for $\epsilon \neq 0$, along) the field lines.

We have calculated the self-consistent potential profile $\Phi(x)$ for representative values of these parameters and the results of this analysis are summarized in Secs. IV and V. We note here that two quite different regimes are found depending on the size of ϵ. For small ϵ, i.e., $\epsilon \lesssim \bar{\nu}$, we find that there is no analog to the Bohm condition for the velocity of the ions incident on the sheath. Moreover, in contrast to the case of an unmagnetized sheath, the sign of the self-consistently determined wall potential, assuming $\Phi = 0$ far from the wall, is not always negative. In fact, it is a strong function of λ, being negative for small λ, positive for large λ, and changing sign for $\lambda \approx 1$. This is illustrated in Fig. 5, where $\Psi_w = e\Phi(x=0)/T_e$ is plotted against λ for the case of large α. The shape of Φ also depends on λ, exhibiting two scale lengths for large λ and a single scale length for small λ. This is shown in Figs. 4(a) and 4(b), where Ψ and $\ln(\Psi/\Psi_w)$ are plotted against $\xi = x/r_{ci}$ for several values of λ, again for large α. (Similar results for smaller values of α are shown in Figs. 9 and 10.) In Fig. 4(c), we show the ion density profiles associated with the potential profiles of Fig. 4(a). Except for the case of positive wall potentials, and then only in the immediate vicinity of the wall, where there is an excess of electrons, the electron and ion density profiles are indistinguishable on the scale used in Fig. 4(c). Finally, we find that the transition from positive to negative wall potentials depends

principally on λ, being only weakly dependent on α and θ, as shown in Figs. 6 and 11.

For large ϵ, we find that a Bohm condition must be satisfied. In addition, as illustrated in Fig. 18, the potential profiles are nearly exponential and only weakly dependent on ϵ, with the scale length decreasing slightly with increasing ϵ on the range $1° < \epsilon < 9°$.

In Sec. II, we describe the technique for calculating the ion density profile, assuming that the potential is a prescribed function of x. In Sec. III, the electron model is discussed, again assuming that the potential is a known function. The ion and electron models are combined with Poisson's equation in Sec. IV and the system of equations is solved self-consistently in the limit of grazing incidence. In Sec. V, we extend our analysis to the case of oblique incidence. Conclusions and a discussion of our results are given in Sec. VI.

II. CALCULATION OF THE ION DENSITY

We begin by considering the ion motion under the combined influence of the magnetic and electric fields,

$$\mathbf{B} = B_0(\hat{\mathbf{z}}\cos\epsilon - \hat{\mathbf{x}}\sin\epsilon) \tag{1}$$

and

$$\mathbf{E} = -\frac{d\Phi(x)}{dx}\hat{\mathbf{x}} + E_y\hat{\mathbf{y}}, \tag{2}$$

where $\mathbf{B}$ is the externally applied magnetic field incident at an angle ϵ on an absorbing wall located at $x=0$ (see Fig. 1); E_y is a constant electric field which models the effects of electrostatic turbulence; and $\Phi(x)$ is the self-consistent sheath potential satisfying Poisson's equation. (For our geometry, outward drift, i.e., toward the wall, corresponds to $E_y < 0$.) In particular, we wish to identify the inadmissible ions, i.e., those which are intercepted by the wall and hence should be omitted from the distribution function when calculating the ion density. Choosing as vector potential for the magnetic field (1)

$$\mathbf{A} = B_0(x\cos\epsilon\hat{\mathbf{y}} - y\sin\epsilon\hat{\mathbf{z}}), \tag{3}$$

we use the Hamiltonian

$$H = \tfrac{1}{2}Mv^2 + e\Phi(x) - eyE_y \tag{4}$$

and the canonical equations of motion as follows. Since $\dot{P}_z = 0$, we have

$$P_z/M \equiv (v_z - \Omega_i y\sin\epsilon) = V_z = \text{const}, \tag{5}$$

where V_z (the average flow velocity along the z axis) is a constant of the motion. The $\dot{P}_y$ equation can be integrated to yield

$$P_y/M \equiv (v_y + \Omega_i x\cos\epsilon) = V_y + \Omega_i v_d t - \Omega_i^2\sin^2\epsilon\int_0^t dt'\, y(t'), \tag{6}$$

where

$$v_d \equiv cE_y/B_0 - V_z\sin\epsilon \tag{7}$$

is the net outward drift (due to $\mathbf{E}\times\mathbf{B}$ and the oblique angle of incidence), and V_y is another constant of motion. Finally, the $\dot{P}_x$ equation can be integrated to give

$$y\cos\epsilon = \frac{1}{\Omega_i}\left(V_x + v_x - \frac{e}{M}\int_0^t dt'\, E_x[x(t')]\right), \tag{8}$$

where V_x is a third constant of motion, and $E_x = -d\Phi/dx$. Then,

$$H = \frac{M}{2}\left[v_x^2 + \left(V_y - \Omega_i(x\cos\epsilon - v_d t) - \Omega_i^2\sin^2\epsilon\int_0^t dt'\, y(t')\right)^2\right] + e\Phi + \frac{M}{2}(V_z + \Omega_i y\sin\epsilon)^2 - eyE_y. \tag{9}$$

Neglecting terms of order ϵ^2 and additive constants, we can replace the last two terms of (9) by

$$v_d\left(e\int_0^t dt'\, E_x[x(t')] - Mv_x\right) \tag{10}$$

and thus write

$$H = \frac{M}{2}(v_x - v_d)^2 + U(x,t,\mathbf{V}), \tag{11}$$

where

$$U(x,t,\mathbf{V}) = \frac{M}{2}[V_y - \Omega_i(x - v_d t)]^2 + e\Phi + v_d e\int_0^t dt'\, E_x[x(t')] \tag{12}$$

serves as an effective (time-dependent) potential for the motion along x.

If the effective potential, U, has the form of a simple potential well, i.e., has a single minimum somewhere to the right of the wall (a situation that we find, *a posteriori*, to cover most cases of interest), a simple, approximate criterion for ion admissibility can be derived, as follows. Although H, as given by (11) and (12), is an explicit function of time, we know that its value is constant if $x(t)$ and $v_x(t)$ satisfy the equations of motion. Consider, then, an ion located at x at time t, which has velocity v_x in the x direction and given values of the constants of motion $\mathbf{V}$. It is inadmissible if, at any earlier time $t' < t$, it was at the wall ($x=0$). Let v_x' be its velocity at t'. Then the constancy of H requires that

$$\frac{M}{2}(v_x' - v_d)^2 + U(0,t',\mathbf{V}) = \frac{M}{2}(v_x - v_d)^2 + U(x,t,\mathbf{V}). \tag{13}$$

If, for all $t' < t$,

$$\Delta U \equiv U(0,t',\mathbf{V}) - U(x,t,\mathbf{V}) > 0 \tag{14}$$

and

$$(v_x - v_d)^2 < 2\Delta U/M \tag{15}$$

then (13) cannot be satisfied. The ion in question could never have been at the wall and hence is admissible; otherwise, it is inadmissible.

While (15) appears to provide a simple criterion for admissibility, it is not easy to use in practice for two reasons. First, U, as given by (12), is a functional of $x(t)$ so that evaluation of $U(x,t,\mathbf{V})$ would still require knowledge of the whole past orbit. In addition, we would have to compute $U(x,t',\mathbf{V})$ for all past t'. We resolve these difficulties by introducing two approximations, to be verified *a posteriori*.

(1) Due to the obliqueness of the magnetic field and to the drift induced by E_y, an ion which originates in the plasma interior (i.e., at large x) will gyrate about a guiding center which is moving toward the wall. (In fact, all such ions will eventually hit the wall, but admissibility of a phase-space point only requires that an ion presently at that point should not have encountered the wall in the past.) If an ion would not have hit the wall during the previous gyration period (i.e., in a time of order $T=2\pi/\Omega_i$), we can assume that it would not have done so at any earlier time, since the guiding center motion is toward the wall. Thus, we may restrict the t' values in (15) to the interval $t-T<t'<t$. We simplify further by choosing $t'=t-T/2$ as a representative time and evaluating $U(t')$ there. Calculations with exact orbits show that with this approximation a small number of inadmissible ions are incorrectly labelled as admissible, and *vice versa*, but these two mislabeled groups are nearly equal in number so the resulting ion density is very close to its correct value.

(2) The last term in (12) contributes to ΔU a term proportional to $-\int_{t-T/2}^{t} dt'\, E_x[x(t')]$, and we approximate this by $-E_x(x)T/2$. With these two approximations, the admissibility condition (15) becomes

$$\frac{M}{2}(v_x-v_d)^2 \leqslant M\Omega_i v_y\left(x-\frac{\pi v_d}{\Omega_i}\right)+\frac{M\Omega_i^2}{2}\left(x-\frac{\pi v_d}{\Omega_i}\right)^2 +e\tilde{\Phi}-\frac{\pi v_d}{\Omega_i}eE_x(x), \tag{16}$$

where $\tilde{\Phi}=\Phi(0)-\Phi(x)$.

To check on the accuracy of this procedure we have used an iterative approach, in which the potential $\Phi(x)$, found using the approximate admissibility condition (16), is used to calculate the exact ion orbits. From these we are able to find the exact velocity space "loss boundary" (between admissible and inadmissible ions) in the approximate sheath potential. As shown in Fig. 2, for $v_d \ll v_{ti}$, the agreement between the actual and approximate loss boundaries is quite good; even for $v_d/v_{ti}=0.1$ the error, while non-negligible, tends to be self-compensating. In addition, we have used the approximate potential to verify that the effective potential indeed has a simple well topology.

In the following analysis, it is convenient to introduce the dimensionless variables

$$\Psi=e\Phi/T_e, \quad \mathscr{E}=eE_x r_{ci}/T_e, \quad \xi=x/r_{ci},$$

$$\theta=T_e/T_i, \quad \mathbf{u}=\mathbf{v}/v_{ti}.$$

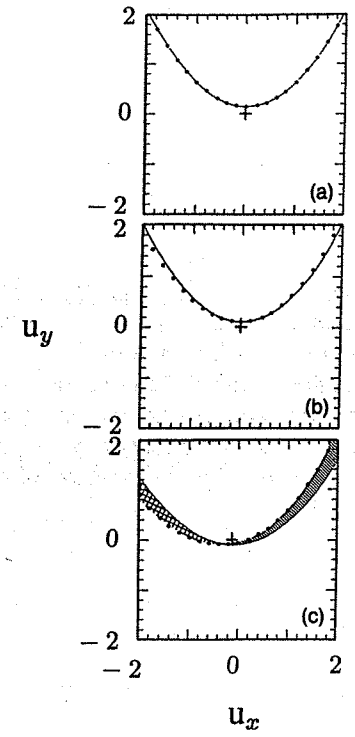

FIG. 2. Comparison of the actual loss boundary (●) and the approximate loss boundary in the test field $\Psi=-2e^{-\xi}$ for the cases (a) $v_d/v_{ti}=0$, (b) $v_d/v_{ti}=0.01$, and (c) $v_d/v_{ti}=0.1$. The cross-hatched area represents particles that should be counted but are missed. The slash-marked area represents particles that are counted but should not be.

In terms of these variables, the admissibility condition (16) becomes

$$(u_x-u_d)^2 \leqslant 2(\xi-u_d\pi)[u_y-u_{y0}(\xi)], \tag{17}$$

where

$$u_{y0}(\xi)=-\left(\frac{(\xi-\pi u_d)^2+\theta\tilde{\Psi}-\theta u_d\mathscr{E}}{2(\xi-\pi u_d)}\right) \tag{18}$$

and $u_d=cE_y/(v_{ti}B_0)-u_z\sin\epsilon$. For fixed ξ, the admissible phase space points all fall within the interior of a parabola in the u_x, u_y plane. We also note that since we have assumed that $u_d \ll 1$, the drifts do not significantly modify the loss boundary except when ξ is comparable to u_d, i.e., in the immediate vicinity of the wall.

In order to find the ion density profile, we need to make an assumption as to the form of the equilibrium ion distribution function. For this, we choose a Maxwell–Boltzmann in perpendicular energy, and a cold beam along the field, i.e.,

$$f_{0i}=\frac{N}{\pi v_{ti}^3}\exp(-H_0)\delta(u_z-u_{z0}), \tag{19}$$

where N is the constant density far from the wall,

$$H_0=(u_x-u_d)^2+u_y^2+\theta\Psi(\xi) \tag{20}$$

is the dimensionless energy at $t=0$, and u_{z0} is the normalized flow velocity along the field. So far as the value of u_{z0} is concerned, we find that for $\epsilon \ll \bar{\nu}$, the sheath structure is

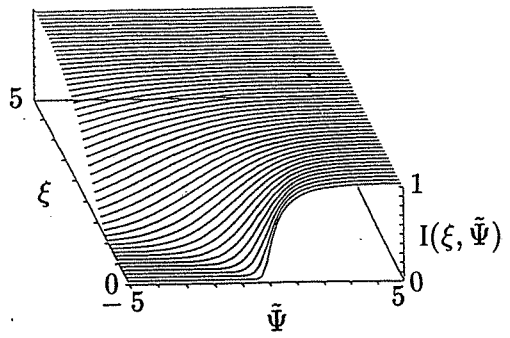

FIG. 3. Plot of the ion loss function $I(\xi,\tilde{\Psi})$ for the range $-5\leqslant[\tilde{\Psi}=q(\Phi_w-\Phi)/T_e]\leqslant 5$, and $0\leqslant(\xi=x/r_{ci})\leqslant 5$.

insensitive to the value of u_{z0} so long as $u_{z0}\ll 1/\epsilon$. For $\epsilon\gtrsim\bar{\nu}$, Chodura demonstrated that sheath stability requires $u_{z0}\simeq 1$. Since the loss boundary in velocity space is a function of the parallel velocity through the quantity u_d, the choice of (19) for the parallel distribution function significantly simplifies the evaluation of the ion density. We find that replacing the delta function in u_z with a distribution having a thermal spread on the order of the perpendicular temperature causes no significant changes in the results.

The ion density is found by integrating the distribution function (19) over the admissible regions of velocity space, i.e., those regions that fall within the loss parabola,

$$n_i(\xi)=\mathrm{N}e^{-\theta\Psi}\frac{2}{\pi}\int_{u_{y0}}^{\infty}du_y\,e^{-u_y^2}\int_{-\infty}^{\infty}du_z \times\delta(u_z-u_{z0})\int_0^{\mathbb{U}}d\tilde{u}_x\,e^{-\tilde{u}_x^2}, \tag{21}$$

where $\tilde{u}_x=u_x-u_d$, and $\mathbb{U}=\sqrt{2(\xi-\pi u_d)[u_y-u_{y0}(\xi)]}$. Carrying out the integrations over u_z, and $\tilde{u}_x$, we find that

$$g_i(\xi)\equiv\frac{n_i(\xi)}{N}=e^{-\theta\Psi}I(\xi,\tilde{\Psi}), \tag{22}$$

where

$$I(\xi,\tilde{\Psi})\equiv\frac{1}{\sqrt{\pi}}\int_0^{\infty}du e^{-(u+u_{y0})^2}\,\mathrm{erf}[\sqrt{2(\xi-\pi u_d)u}]. \tag{23}$$

Thus the ions have a Boltzmann distribution, modified by the function, $I(\xi,\tilde{\Psi})$, which accounts for the particles which are removed by the wall. A graphical representation of I is shown in Fig. 3.

It is important to note that the primary function of the ion flow out of the plasma, as far as the calculation of the ion density profile is concerned, is to partially fill in the ion loss region. Provided that u_d is sufficiently small, as in the case of grazing incidence (Sec. IV), we may neglect finite u_d effects in evaluating the ion loss function without changing the results of the sheath calculation. On the other hand, if the ion flow along the field becomes large, as in the case of oblique incidence (Sec. V), it is necessary to retain the finite u_d effects in the ion loss function since the filling in of the ion loss region can be significant and hence can alter the results of the sheath calculation. Of course, in either case the ion and electron flows out of the plasma must be equal.

III. THE ELECTRON MODEL

Since the electron gyroradius is typically very small compared to all other scale lengths of the system, it is appropriate to describe the electrons using warm fluid equations, including the effects of electron–neutral collisions. Assuming that the fluid velocity is much less than the electron thermal velocity, and that all gradients are normal to the wall, these equations reduce in steady state to

$$\frac{d}{dx}(n_e v_{ex})=0, \tag{24}$$

$$T_e\frac{dn_e}{dx}\hat{\mathbf{x}}+en_e\left[\left(-\frac{d\Phi(x)}{dx}\hat{\mathbf{x}}+E_y\hat{\mathbf{y}}\right)+\frac{B_0}{c}[\mathbf{v}_e\times(\hat{\mathbf{z}}\cos\epsilon-\hat{\mathbf{x}}\sin\epsilon)]\right]+\nu mn_e\mathbf{v}_e=0, \tag{25}$$

where ν is the electron–neutral collision frequency and we have neglected particle sources in the sheath region. Eliminating v_{ey} and v_{ez} from (25) we obtain an equation relating the electron flux, $\Gamma_x\equiv n_e v_{ex}$, to the electric field and the density gradient,

$$\Gamma_x=-D_e(\epsilon^2+\bar{\nu}^2)\left(\frac{dn_e}{dx}-\frac{e}{T_e}n_e\frac{d\Phi}{dx}\right)+\frac{E_y c}{B_0}n_e, \tag{26}$$

where $D_e=T_e/m\nu$ and we have assumed that $\bar{\nu}\equiv\nu/\Omega_e\ll 1$ and $\epsilon\ll 1$. The first term in (26) represents the classical cross-field diffusion and mobility due to electron–neutral collisions, while the second term accounts for the $\mathbf{E}\times\mathbf{B}$ drift due to fluctuations (here modeled by a constant E_y field).

Equation (26) is to be solved for the electron density in terms of the electrostatic potential, subject to the boundary conditions that far from the wall, where $d\Phi/dx$ approaches zero, the density approaches the constant value N. Since (24) implies that $\Gamma_x=$const, we have from (26)

$$\Gamma_x(x)=\Gamma_x(\infty)=N\frac{E_y c}{B_0}, \tag{27}$$

i.e., the flux out of the plasma is determined by the internal density and the effective "turbulent" electric field. In terms of the dimensionless variables

$$\Psi=e\Phi/T_e,\quad g_e=n_e/N,\quad \xi=x/r_{ci},\quad u_E=cE_y/Bv_{ti}, \tag{28}$$

and

$$\lambda=-\left|\left(\frac{cE_y}{B_0 v_{ti}}\right)\left(\frac{r_{ci}^2\Omega_i}{D_e(\epsilon^2+\bar{\nu}^2)}\right)\right|=\frac{2u_E\bar{\nu}}{\theta(\epsilon^2+\bar{\nu}^2)}$$

which measures the relative magnitudes of the two terms in (26) that equation becomes

$$\frac{dg_e}{d\xi}+g_e\frac{d}{d\xi}[\lambda\xi-\Psi(\xi)]=\lambda. \tag{29}$$

Combining this equation with the expression for the ion density derived in the previous section, Poisson's equation, and a proper set of boundary conditions allows us to find the self-consistent potential and density functions for the grazing incidence magnetic sheath. This will be carried out in Sec. IV.

Before turning to this, we note that λ is a very sensitive function of the angle of incidence near $\epsilon=0$, since $\lambda(\epsilon=0)/\lambda(\epsilon=\epsilon_0)=1+(\epsilon_0/\bar{v})^2$ and typically $\bar{v}\ll 1$. As a specific example, consider a hydrogen plasma with a background neutral density of $n_n=10^{13}$ cm^{-3}, magnetic field $B_0=10^4$ G, temperature $T_e=T_i=10$ eV, and an outward fluctuation-induced ($\mathbf{E}\times\mathbf{B}$) particle drift with $u_E=10^{-2}$. If we assume an electron–neutral collision cross section of 5×10^{-15} cm^2, then for these parameters $\bar{\nu}=3.8\times10^{-5}$, and thus for $\epsilon=0$, $\lambda=5.3\times10^2$, whereas for $\epsilon=1°$, $\lambda=2.5\times10^{-3}$. This strong dependence of λ on the angle of incidence is important because solutions of Eq. (29), and hence of Poisson's equation, have greatly different characteristics in the limits of $\lambda\gg1$ and $\lambda\ll1$. In particular, it can be shown that in the limit $\lambda\gg1$ (convective loss), $g_e=1$ to lowest order in $1/\lambda$, whereas for $\lambda\ll1$ (diffusive loss), $g_e=e^{\Psi}$ to lowest order in λ. Thus, as ϵ is varied from zero to one degree, the electron density changes from an essentially uniform distribution to a Boltzmann distribution. It is, therefore, necessary to carry out the analysis in such a way as to accommodate a wide range of λ values.

IV. THE MAGNETIZED SHEATH: GRAZING INCIDENCE

In the previous two sections, we derived an algebraic expression for the ion density and a differential equation for the electron density, treating the electrostatic sheath potential as a known function of position. We now combine these results with the one dimensional Poisson's equation, which we write in dimensionless form,

$$\frac{d^2\Psi}{d\xi^2}=\alpha^2(g_e-g_i), \tag{30}$$

where

$$\alpha^2=k_D^2r_{ci}^2=\left(\frac{4\pi Ne^2}{T_e}\right)\left(\frac{2T_i/M}{\Omega_i^2}\right). \tag{31}$$

In the limit $T_e=T_i$, the parameter α^2 may be expressed as $\alpha^2=2(\omega_{pi}/\Omega_i)^2=8\pi NMc^2/B^2$. (For fusion plasmas $\alpha^2=200n_{12}/\theta B_T^2\gg1$, where $n_{12}=10^{12}n_e$ is the electron density in units of 10^{12} cm^{-3}, and B_T is the magnetic field in Teslas, so we shall often consider the limit of large α^2.) Instead of solving for g_e and g_i in terms of Ψ [the former requiring solution of the differential equation (29)], substituting these in (30), and solving (30) for Ψ, we find it useful to solve (30) for g_e in terms of Ψ and $g_i(\Psi)$, and substitute this into (29). This leads to a nonlinear third-order differential equation in Ψ,

$$\frac{1}{\alpha^2}\left[\frac{d^3\Psi}{d\xi^3}+\left(\lambda-\frac{d\Psi}{d\xi}\right)\frac{d^2\Psi}{d\xi^2}\right]+\left[\frac{dg_i}{d\xi}+g_i\left(\lambda-\frac{d\Psi}{d\xi}\right)-\lambda\right]=0, \tag{32}$$

which requires specification of three boundary conditions. Two of these have already been used in deriving the expressions for the charge densities, since we have assumed that far from the wall both the potential and the electric field approach zero. A natural choice for the third boundary condition follows if we assume strict charge neutrality, $n_e=n_i$, deep in the plasma interior. Thus our three internal boundary conditions are

$$\Psi(\xi\to\infty)=0,\quad \left.\frac{d\Psi}{d\xi}\right|_{\xi\to\infty}=0,\quad \left.\frac{d^2\Psi}{d\xi^2}\right|_{\xi\to\infty}=0. \tag{33}$$

Although the differential equation (32) and boundary conditions (33) uniquely determine Ψ, for given λ, there is one technical complication. Calculation of the ion loss function I, which enters into the determination of g_i, requires specification of the wall potential Ψ_w, and this is not known until $\Psi(\xi)$ has been determined. We therefore use an iterative procedure: choose values for Ψ_w and λ; numerically integrate (32), starting at some large value $\xi=\xi_{\max}$, where (33) is assumed to be satisfied; compare the resultant $\Psi(0)$ with Ψ_w; and vary λ until $\Psi(0)$ equals Ψ_w.

An interesting feature of the magnetized sheath in the grazing incidence regime is exhibited by examining equation (32) in the asymptotic region $|\xi|\gg1$, where Ψ and all of its derivatives are small and nonlinear terms can be neglected. In this region, we may also neglect ion losses to the wall, i.e., set $I(\xi,\Psi)=1$ (cf. Fig. 3), so the ion density profile reduces to $g_i=e^{-\theta\Psi}\approx1-\theta\Psi$. Using these approximations, we have for (32)

$$\frac{d^3\Psi}{d\xi^3}+\lambda\frac{d^2\Psi}{d\xi^2}-\alpha^2(1+\theta)\frac{d\Psi}{d\xi}-\lambda\theta\alpha^2\Psi=0. \tag{34}$$

The solutions to this linear equation are $\exp(r\xi)$, where r is a solution of a cubic equation whose roots, for large α, are $-\theta\lambda/(1+\theta)$ and $\pm\alpha(1+\theta)^{1/2}$. Therefore, the general solution of (34) consistent with (33) is

$$\Psi(\xi)=\mathbb{C}_1\exp\left[-\left(\frac{\theta\lambda}{1+\theta}\right)\xi\right]+\mathbb{C}_2\exp[-(\sqrt{1+\theta}\alpha)\xi], \tag{35}$$

where $\mathbb{C}_1$ and $\mathbb{C}_2$ are constants of integration. We note that in contrast with the unmagnetized sheath result, there is no requirement on the incoming flow velocity of the ions in order to obtain "sheathlike" solutions, i.e., there is no equivalent to the Bohm condition for the grazing incidence sheath. In the unmagnetized sheath model the plasma ions are accelerated to sonic velocity in a presheath region before entering the actual sheath. In our model of the magnetized sheath for grazing incidence, the presheath region is replaced by a region of constant density and fixed effective electric field (fluctuation level) so that the plasma particles enter the sheath with a constant flux.

We now consider the full nonlinear sheath equation (32), again assuming $\alpha^2\gg1$ so that Ψ can be expanded in inverse powers of α^2,

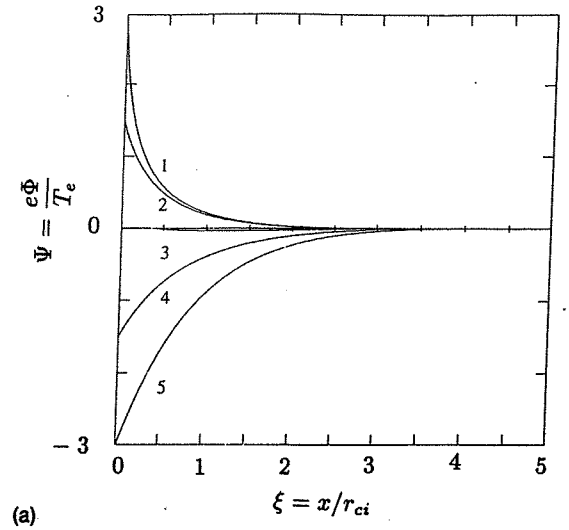

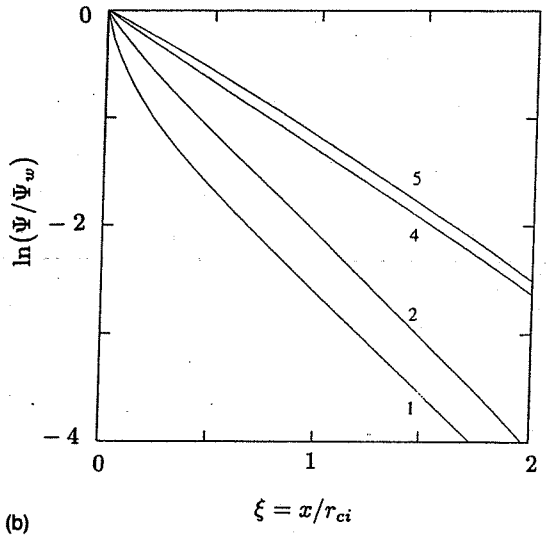

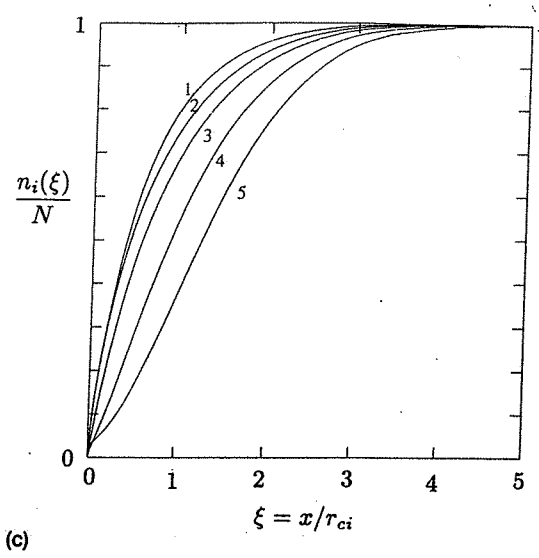

FIG. 4. (a) Potential profiles in the limit of large α for the cases $\theta=1$ and (1) $\lambda=3.15$; (2) $\lambda=2.35$; (3) $\lambda=1.21$; (4) $\lambda=0.42$; and (5) $\lambda=0.063$. (b) Logarithmic plot of the normalized potential profiles corresponding parameters in (a). Note that case 3 has not been included since it is not a monotonic function and that the range in ξ has been limited to the first two gyroradii beyond the wall to better show the short scale length region for large λ. (c) Ion density profiles corresponding to parameters in (a).

$$\Psi=\sum_{j=0}^{\infty}\left(\frac{1}{\alpha^2}\right)^j\Psi_j. \tag{36}$$

To lowest order in $1/\alpha^2$, we have

$$\frac{dg_i}{d\xi}+g_i\left(\lambda-\frac{d\Psi}{d\xi}\right)-\lambda=0. \tag{37}$$

Comparing (37) with (29), we see that this approximation is essentially the same as requiring the plasma to remain quasineutral. This result may also be obtained directly by combining (29) and (30) while neglecting terms of order $1/\alpha^2$. Using equation (22) for the ion density, gives

$$(1+\theta)I\frac{d\Psi}{d\xi}-\frac{dI}{d\xi}+\lambda(e^{\theta\Psi}-I)=0. \tag{38}$$

Finally, since the spatial derivative of I can be expressed in the form

$$\frac{dI}{d\xi}=H-\theta J\frac{d\Psi}{d\xi}, \tag{39}$$

where H and J are also known functions of ξ and Ψ (cf. the Appendix), we obtain the first-order equation

$$\frac{d\Psi}{d\xi}=\frac{H+\lambda I-\lambda e^{\theta\Psi}}{(1+\theta)I+\theta J}. \tag{40}$$

Some typical results for the potential profiles resulting from numerical integration of (40) with $\theta=1$, are shown in Fig. 4(a). In Fig. 4(b), we have plotted $\ln(\Psi/\Psi_w)$ as a function of ξ in the neighborhood of the wall to bring out the essential features of the scale lengths. We note that in the case of negative wall potentials, (cases 4 and 5) the sheath is characterized by a single scale length on the order of the ion gyroradius. In the case of positive wall potentials (cases 1 and 2), however, the sheath is characterized by two scale lengths: (1) a short scale length, which is a decreasing function of λ, adjacent to the wall followed by a longer scale length (again of order r_{ci}, *albeit*, somewhat shorter than the negative wall potential case) in the interior. Physically, this difference in the scaling for positive and negative potentials is related to the structure of the ion loss function. If the wall potential is positive it acts to reflect the majority of the ions back into the plasma; hence, except for distances much less than an ion gyroradius, the majority of the ions are confined and the ion loss function

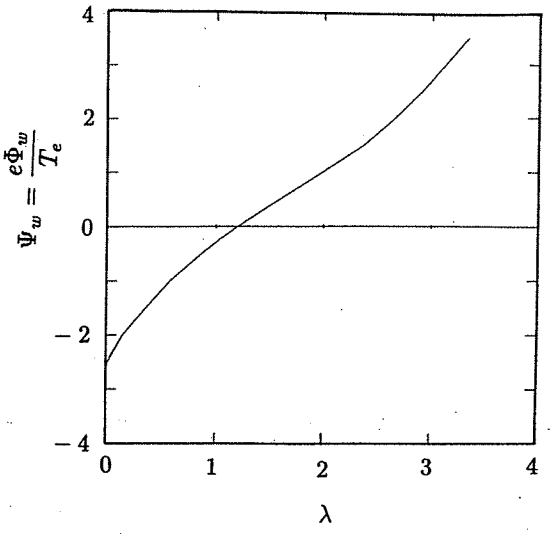

FIG. 5. Calculated wall potential as a function of $\lambda \equiv 2u_E\bar{\nu}/\theta(\bar{\nu}^2+\epsilon^2)$ in the limit of large α, and for $\theta=1$.

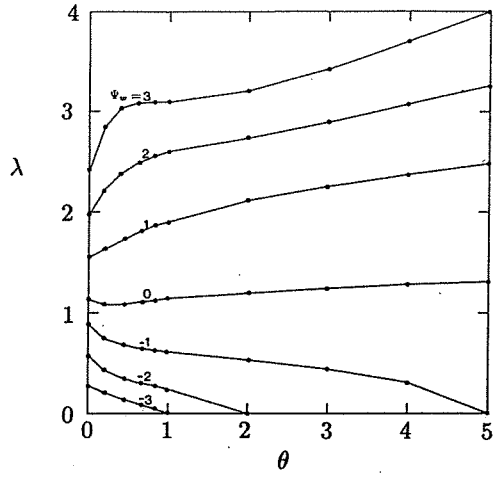

FIG. 6. Contours of constant wall potential as a function of θ and λ in the limit of large α.

has a value close to unity. In the immediate vicinity of the wall, where the ion population is severely depleted, the ion loss function is a rapidly increasing function of ξ. In order for the electron density to vary on the same scale length (as required when α is large since this implies quasineutrality), the potential rise must also have a very short scale length near the wall. On the other hand, when the wall potential is negative, ions can be lost from distances on the order of an ion gyroradius, resulting in a potential drop on a longer scale length, or order r_{ci}. In Fig. 4(c) we have plotted the ion density profiles corresponding to the potential profiles of Fig. 4(a). Except for the case of large λ, and then only in the immediate vicinity of the wall, where there is an excess of electrons, the electron density profile is indistinguishable from the ion density profile on this scale.

In Fig. 5, we have plotted the wall potential as a function of the parameter λ in the limit of large α, again for $\theta=1$. The potential changes sign near $\lambda=1$, a result most easily understood by regarding $u_E=E_y c/B_0 v_{ti}$ as constant. From (28) it then follows that small λ corresponds to large values of D_e, the diffusion coefficient, and hence to a situation in which the electrons are free to diffuse out of the plasma. To balance the electron and ion fluxes requires a negative electric field, i.e., one which tends to retard the electron flow, and this corresponds to a negative wall potential. For large λ, the situation is reversed: The electrons are well confined (D_e is small) so equality of electron and ion fluxes requires an electric field which enhances the electron flow, corresponding to a positive wall potential.

Using the fact that the potential changes sign for $\lambda \approx 1$, we may solve (28) for ϵ to find the angle at which the potential change should occur for any given interior conditions, i.e.,

$$\epsilon=\bar{\nu}\left[\left(\frac{2u_E}{\theta\bar{\nu}}\right)-1\right]^{1/2}. \tag{41}$$

(If, as in Sec. III, we consider the edge region of a typical tokamak to be characterized by the quantities $u_E=10^{-2}$, $T_e=T_i=10$ eV, $B_0=10^4$ G, and $n_n=10^{12}$–10^{14} cm^{-3}, this implies that the wall potential will change sign for $0.01° < \epsilon < 0.25°$. Since in most tokamaks, the magnetic field lines intercept the limiter with an angle on the order of 6°, it is unlikely that the grazing incidence case will be observed in this environment. This is fortunate, since it indicates that the sheath may be correctly modeled by the much more robust structure of the oblique incidence case for advanced applications such as modeling wall sputtering, recycling, and transport.)

Allowing unequal ion and electron temperatures ($\theta \neq 1$) results in potential profiles which differ only slightly from those for $\theta=1$. Some aspects of this are illustrated in Fig. (6) which shows contours of constant wall potential Ψ_w as a function of θ and λ. Since the $\Psi_w=0$ contour is nearly independent of θ, it follows that the transition from positive to negative sheath potentials depends principally on λ. We also see that for $\theta > 1$ there are no solutions with large negative wall potentials, i.e., $\Psi_w < -3$. In Figs. 7 and 8, we have plotted the potential profiles for fixed wall potentials ($\Psi_w=3$ and $\Psi_w=-1$) with $\theta=0.2$, 1, and 5. The interesting feature of these results is that for negative Ψ_w, increasing θ tends to increase the scale length of the sheath, whereas for positive Ψ_w, increasing θ tends to decrease the scale length. This behavior is consistent with our previous discussion of the physics governing the sheath scale length, since the potential in the ion loss function is multiplied by θ.

Finally, we consider the finite α (i.e., charge separation) corrections to the infinite α approximations discussed in the preceding paragraphs. This requires solution of the full magnetized sheath equation (32), i.e., a nonlinear third-order differential equation. Since the coefficient of the highest derivative is small (assuming $\alpha \gg 1$), it is appropriate to use a boundary layer analysis. In the plasma interior ($\xi \gg 1$) where the gradients are small, we approximate (32) by its large α form (37), and match solutions of (37) to

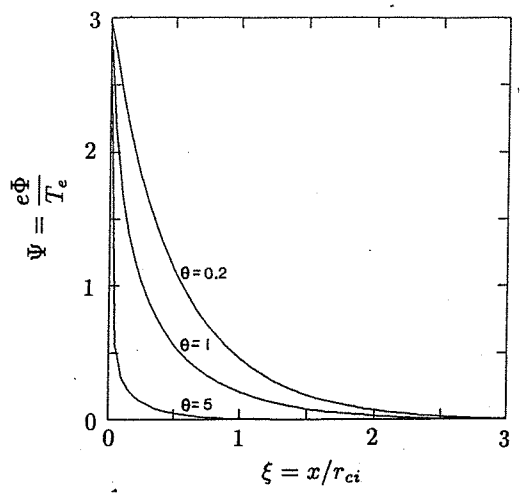

FIG. 7. Sheath potential profiles for the case $\Psi_w=3$ and $\theta=0.2$, 1, and 5 in the limit of large α.

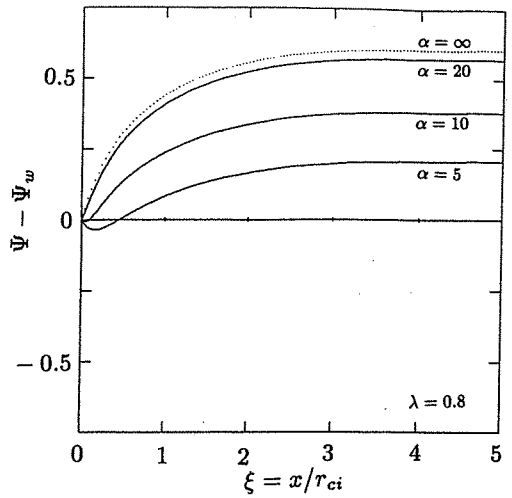

FIG. 9. Sheath potential profiles for $\theta=1$, $\lambda=0.8$, and $\alpha=5$, 10, 20, and ∞.

those of (32) at some suitably chosen matching point. The results of this calculation, whose details are described in Ref. 6, are shown in Figs. 9 and 10 for $\alpha=5$, 10, 20, and ∞ and two values of λ, $\lambda=0.8$ and $\lambda=2.67$. We see that the potential profiles are vitually independent of α for $\lambda=2.67$, but show a significant α dependence for $\lambda=0.8$. Physically, this result arises because the $1/\alpha^2$ terms correspond to charge separation effects. Since the larger λ results predict a larger potential gradient and hence a larger charge separation even for the case of large α, the $1/\alpha^2$ corrections do not produce a significant change. For the smaller λ case, however, the potential gradient is small, and the plasma tends to be quasineutral all the way up to the wall. Thus even a small contribution to the charge separation can produce a relatively large change in the potential profile. In Fig. 11, we have plotted contours of constant wall potential as a function of α and λ. Since the contours for which $|\Psi_w|=0.1$ are virtually independent of α, the same is true for the value of λ for which the potential changes sign.

Having determined the equilibrium sheath profiles, we are now able to verify, *a posteriori*, several approximations made in the course of our analysis. In calculating the ion density, we assumed that the effective potential for the ion motion had a single minimum at some distance from the wall. In Fig. 12, we show the effective potential in the limit of large α for the cases $\Psi_w=-3$, and $V_y=1.3$, 1.5, and 1.7. The values of V_y were chosen so as to show the transition from no confined particles (i.e., no local minimum) to the case of a single minimum. Since in the transition we find no evidence of a local maximum to the right of the wall, we conclude that our assumption of a simple well topology was indeed correct. Our second major approximation was that the inclusion of fluctuation-induced transport and finite angle effects has only a small impact on the evaluation

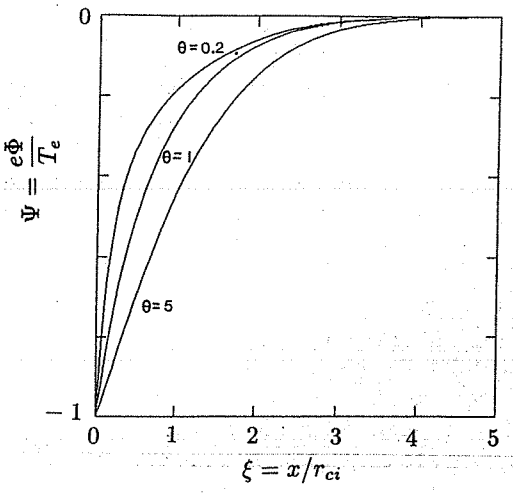

FIG. 8. Sheath potential profiles for the case $\Psi_w=-1$ and $\theta=0.2$, 1, and 5 in the limit of large α.

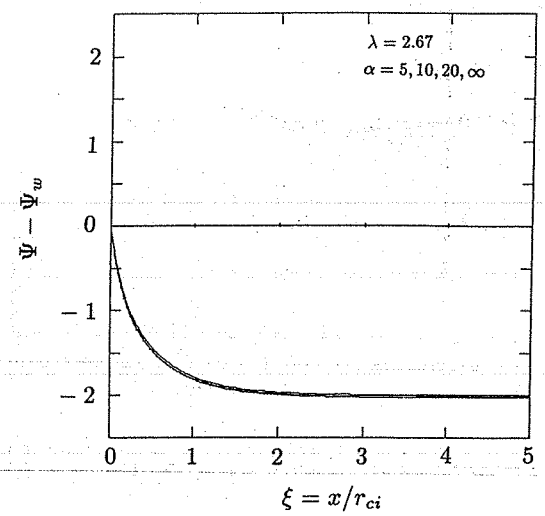

FIG. 10. Sheath potential profiles for $\theta=1$, $\lambda=2.67$, and $\alpha=5$, 10, 20, and ∞.

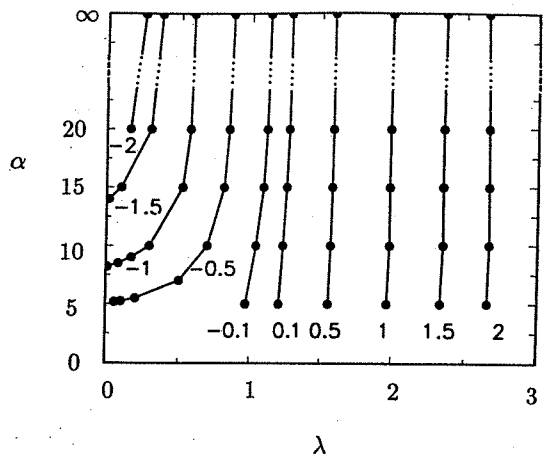

FIG. 11. Contours of constant wall potential as a function of α and λ for $\theta=1$.

of the ion loss boundary. In Fig. 13, we show the approximate ion loss boundary found from evaluating (16), (solid line) and the loss boundary found by following ion trajectories in the calculated sheath field, (dots) for the cases $\Psi_w=-2$, $\alpha=5$, $\theta=1$, and $\xi=1$ and 0.25. As can be seen, the agreement in these cases is excellent.

We conclude this section by comparing our results with those of previously published models. Perhaps the most closely related theory is the pioneering work of Daybelge and Bein.[1] In their analysis, the authors use a model analogous to the ion model presented in Sec. II of this paper for both charge species. Since in their numerical work, the field was taken to be perfectly parallel to the wall ($\epsilon=0$), and since they did not allow for collisional effects, there was no mechanism to allow for plasma flow to the

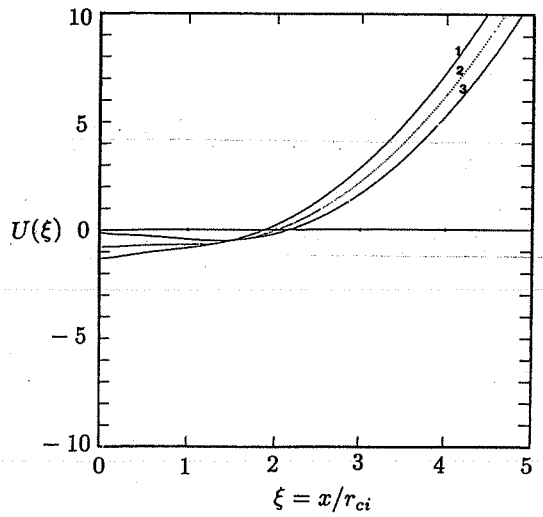

FIG. 12. Effective potential profiles for $\Psi_w=-3$, $\theta=1$, and $V_y=(1)$ 1.7, (2) 1.5, and (3) 1.3 in the limit of large α. The three curves have been chosen so as to show the transition from no confined particle (i.e., no local minimum) to a simple well structure. Note that there is no indication of a local maximum developing to the right of the wall, thus confirming our original assumption of the simple well topology.

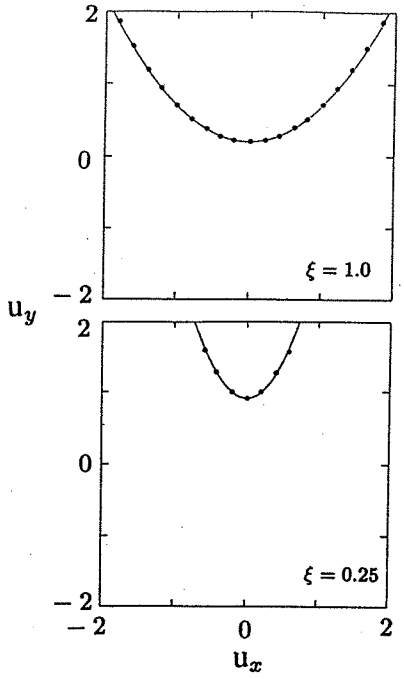

FIG. 13. Comparison of the actual loss boundary (●) found by following ion trajectories back in time with the approximate ion loss boundary used in calculating the potential profile for the cases $\Psi_w=-2$, $\alpha=5$, $\theta=1$, and $\xi=1$ and 0.25.

wall and consequently no way to self-consistently determine the wall potential. They simply assume a value for the wall potential and solve Poisson's equation subject to the additional boundary condition that the potential asymptotes to zero far from the wall. Since the density profile for particle of a given species is affected by the wall over distances on the order of that species' gyroradius (i.e., the particle loss function is less than unity only for distances on the order of a gyroradius), and since the electron gyroradius is taken to be vanishingly small, the electrons, in their analysis, are well modeled by a Boltzmann distribution all the way to the wall, i.e., $g_e \simeq e^{\Psi}$. We note that this corresponds precisely with our model in the limit $\lambda \to 0$. Recalling that, in this case, our model predicts large negative wall potentials, we would expect that in this regime the two theories have similar results, but that the results would begin to diverge for less negative wall potentials, where the finite λ corrections to the electron density become important in our model. This is indeed the case, as is shown in Fig. 14, where we have plotted sheath potential profiles as determined by the two theories for the cases $\alpha=43$ and $\Psi_w=-1$, -2, and -3.

In a recent series of two articles, Theilhaber and Birdsall[2,3] presented the results of 1- and 2-D particle simulations for the magnetized plasma sheath for the case $\epsilon=0$. For short-time scales ($t \sim 2\pi/\Omega_{ci}$) they observed that the 1- and 2-D codes produce similar results, but that for long times ($t \gg 2\pi/\Omega_{ci}$) the shear in the cross-field (parallel to the wall) flow of the plasma results in a Kelvin–Helmholtz instability, which drives the plasma into a state of turbulent equilibrium characterized by the presence of a

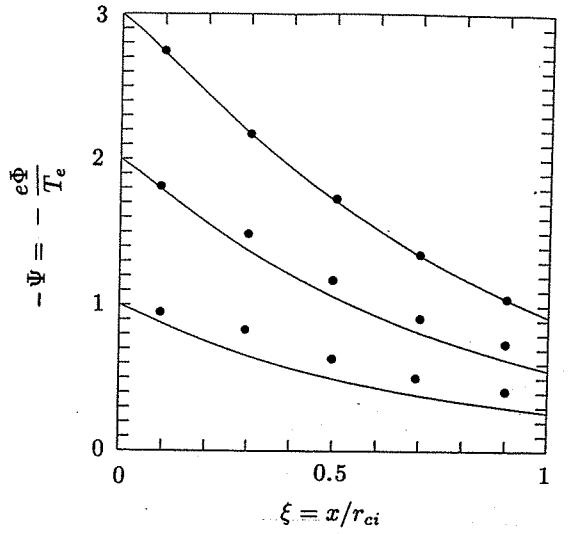

FIG. 14. Comparison of the results of Daybelge and Bein (●) with those of the present theory for the case in which $\Psi_w<0$. Note that for $\Psi_w=-3$ the two theories yield identical results, but that for smaller values of $|\Psi_w|$, where the finite λ corrections become important in our model, the results differ.

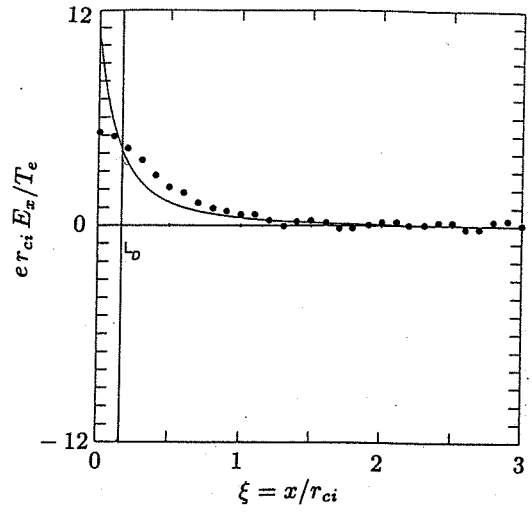

FIG. 15. Comparison of the electric field calculated by Theilhaber and Birdsall's 1-D electrostatic particle in cell code (●) and the present analytic theory (solid line), for the case $\Psi_w=2.5$ and $\alpha=6.3$. The difference in the electric fields near the wall arises from the finite electron gyroradius effects in the PIC code.

large scale ($\sim r_{ci}$), large amplitude ($e\Phi/T_e\sim 1$) vortex traveling in the direction of the cross-field flow at approximately one-half of the ion thermal velocity. In order to run particle simulations for times which are much longer than the ion cyclotron period, an ion to electron mass ratio of 40 was used in the simulations. This causes the electron gyroradius to be of the same order of the Debye length for their parameters, resulting in a depletion of the electron density on the Debye/electron gyroradius scale. Thus, we would not expect their simulation results to correspond well with our theoretical results within a Debye length of the wall. In Fig. 15, we compare the electric field predicted from our model with the time asymptotic result of their 1-D simulation for the cases $\Psi_w=2.5$ and $\alpha=6.3$. As expected, the results are in agreement except within a Debye length of the wall. For the 2-D simulation, the presence of the vortex washes out the shorter scale lengths in the sheath and the two calculations are in poor agreement. Thus, for the cases in which the wall potential is positive with respect to the plasma, we may regard the present model as describing the early time development of the sheath (i.e., the time before the development of the vortex structure). As noted by Theilhaber and Birdsall,[3] even small angles of incidence for the magnetic field [in their simulation $\epsilon=(m_e/M)^{1/2}/8$], results in a sheath in which the electron dynamics dominate, thereby causing the wall potential to be negative with respect to the plasma interior. This is in good agreement with the present model which also predicts a negative wall potential even for small angles of incidence. In addition, by allowing electrons to flow out of the plasma along the magnetic field lines no vortex structures are allowed to develop since the electrons tend to short them out. Hence, we would expect the two models to yield similar results in this regime even for long times.

Finally, in a related paper by Gerver, Parker and Theilhaber,[4] the authors propose *ad hoc* kinetic equations for both the ions and electron distribution functions which enable the modeling of 2-D transport effects in a 1-D code. In the limit of small cross-field diffusion, their results are qualitatively similar to those obtained here (Fig. 16).

V. THE MAGNETIZED SHEATH: OBLIQUE INCIDENCE

If $\epsilon\gg\bar{\nu}$, the value of λ becomes sufficiently small that the electrons are well represented by a Boltzmann distribution, and thus we have algebraic expressions for both charge species. In this case, the most expedient way to obtain the sheath potential is by a direct solution of Poisson's equation,

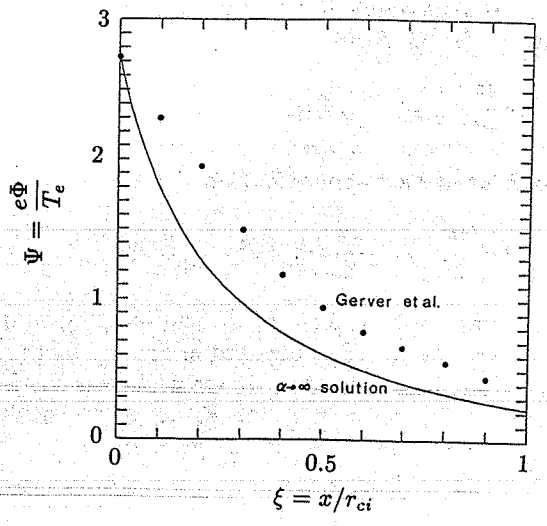

FIG. 16. Comparison of the potential profile from Gerver *et al.*'s 1-D particle in cell code in the limit of no guiding center diffusion with the results of our analytic theory for the case $\Psi_w=2.67$ and $\alpha=6.67$.

$$\frac{d^2\Psi}{d\xi^2}=\alpha^2[e^{\Psi}-e^{-\theta\Psi}I(\xi,\tilde{\Psi})] \tag{42}$$

with two appropriate boundary conditions,

$$\Psi(\xi=0)=\Psi_w, \quad \Psi(\xi\to\infty)=0. \tag{43}$$

There are two aspects of these boundary conditions that are worthy of note. First, since we are in the regime of small λ, Ψ_w will be less than zero. Second, it follows from (42) that if $\Psi(\xi\to\infty)=0$, then $(d^2\Psi/d\xi^2)|_{\xi\to\infty}=0$, and, hence, $(d\Psi/d\xi)|_{\xi\to\infty}\to$a constant value for $\xi\to\infty$. This constant must be zero since Ψ also approaches a constant (namely zero) for $\xi\to\infty$.

In solving (42) and (43) we need to determine two quantities: (1) the flow velocity of the ions into the sheath (i.e., a generalization of the Bohm condition), and (2) the value of the wall potential. The first of these requirements, which arises because the ion loss function, I, depends on the incoming flow velocity, u_z, of the ions [cf. Eq. (18), (22), and (23)], has been addressed by Chodura. His analysis, which we do not reproduce here, shows that to obtain stable sheathlike solutions the ions must be flowing along the field lines at the ion acoustic speed, $C_s\equiv\sqrt{T_e/M}$. Thus, in evaluating I, we use $u_d=cE_y/(v_{ti}B_0)-C_s\sin\epsilon$. In analogy with the unmagnetized sheath, this requirement on the ion flow velocity along the magnetic field mandates the presence of a presheath between the bulk plasma and the actual sheath when the magnetic-field intercepts the wall with oblique incidence.

The potential difference across the sheath [or since $\Psi(\xi\to\infty)=0$ the potential at the wall] is determined by requiring an equal flux of ions and electrons to the wall. Far from the wall, where the particle density has attained the constant value N, Chodura's condition $u_z=C_s$ implies a parallel ion flux

$$\Gamma_{i\|}=-NC_s. \tag{44}$$

To determine the parallel flux of electrons we must first establish a criterion for the determination of their admissible phase-space points. Consider the Lorentz force equation for an electron,

$$m\frac{d\mathbf{v}}{dt}=-e\mathbf{E}-\frac{e}{c}\mathbf{v}\times\mathbf{B} \tag{45}$$

which has the constant of motion

$$H\equiv\frac{mv^2}{2}-e\Phi=\frac{m}{2}[v_{\|}^2+v_1^2+v_2^2]-e\Phi. \tag{46}$$

In writing (46) in terms of its velocity components, we have used the geometry depicted in Fig. (17) with $\mathbf{E}$ normal to the wall. Note that we are neglecting the E_y field, since for this range of ϵ, the $E_y\times B$ drift contributes a negligible amount to the total electron flux as compared to flow along the field. Then

$$\mathbf{B}=B_0\hat{e}_{\|}, \tag{47}$$

$$\mathbf{E}=E(x)\sin\epsilon\,\hat{e}_{\|}+E(x)\cos\epsilon\,\hat{e}_1, \tag{48}$$

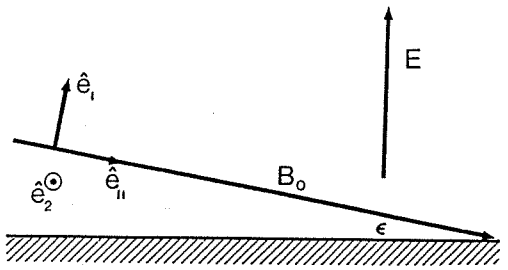

FIG. 17. Coordinate system used for calculating the electron motion.

and the perpendicular components of the Lorentz equation become

$$\frac{dv_1}{dt}=-\Omega_e[v_2+v_E\cos\epsilon], \tag{49}$$

$$\frac{dv_2}{dt}=\Omega_e v_1, \tag{50}$$

where $\Omega_e\equiv eB/mc$ and $v_E\equiv Ec/B$. Assuming that the electron gyroradius is much smaller than the scale length of the electric field, we may treat v_E as constant in evaluating the above equations, which gives

$$v_1=v_{\perp}\cos(\Omega_e t+\phi) \tag{51}$$

and

$$v_2=v_{\perp}\sin(\Omega_e t+\phi)-v_E\cos\epsilon, \tag{52}$$

where $v_{\perp}$ is the constant perpendicular velocity of the electron in the frame drifting with the local $\mathbf{E}\times\mathbf{B}$ velocity, and ϕ is the velocity phase angle of the electron at $t=0$. Substituting these expressions for v_1 and v_2 into (46) and averaging over an electron gyroperiod, yields

$$H\equiv\frac{m}{2}(v_{\|}^2+v_{\perp}^2+v_E^2\cos^2\epsilon)-e\Phi. \tag{53}$$

An electron located far from the wall (i.e., $x\to\infty$), where the potential and the electric field vanish, can escape from the plasma only if its kinetic energy is large enough so that it does not have a turning point in its motion along the field before encountering the wall. Taking into account the constancy of $v_{\perp}$, this implies,

$$v_{\|}^2\geq v_E^2(x=0)\cos^2\epsilon-\frac{2e}{m}\Phi(x=0)=v_{Ew}^2\cos^2\epsilon-\frac{2e}{m}\Phi_w. \tag{54}$$

The parallel electron flux far from the wall is found by integrating the first moment of the electron distribution function subject to the condition that only particles with a velocity which satisfy inequality (54) contribute to the particle loss. Since the majority of the electrons are reflected by the negative wall potential, we assume that the electrons have a Maxwell–Boltzmann distribution and thus find that

$$\Gamma_{e\|}=-\frac{Nv_{te}}{2\sqrt{\pi}}\exp\left(\frac{e\Phi_w}{T_e}-\frac{v_{Ew}^2}{v_{te}^2}\cos^2\epsilon\right). \tag{55}$$

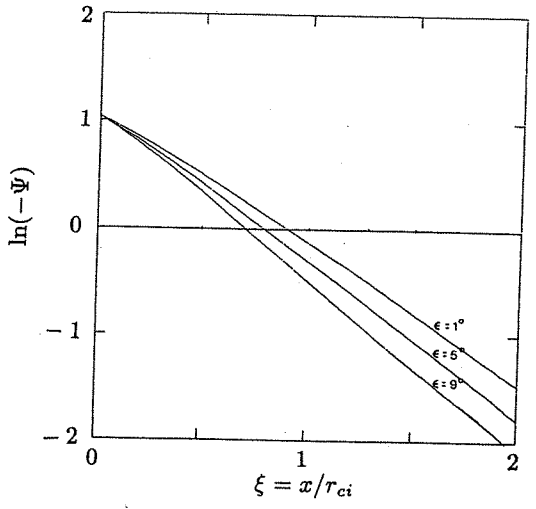

FIG. 18. Logarithmic plot of the magnitude of the potential for the cases $\alpha=5$, $\theta=1$, and $\epsilon=1°$, 5°, and 9°. Note that the potential at the wall is independent of ϵ but that larger ϵ results in a shorter scale length.

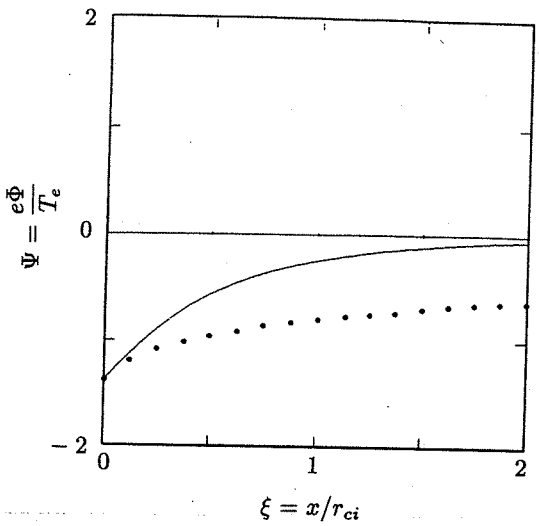

FIG. 19. Comparison of the potential profile from Chodura's particle simulation (●) and our analytic theory (solid line) for the case $M/m=100$, $\alpha=10$, and $\epsilon=10°$.

Equating this to the ion flow along the field, $\Gamma_{i\|} = -NC_s$, and solving for the wall potential yields

$$\frac{e\Phi_w}{T_e} = \frac{1}{2}\ln\left(\frac{2\pi m}{M}\right) + \frac{v_{Ew}^2}{v_{te}^2}\cos^2\epsilon. \tag{56}$$

Note that the leading term on the right-hand side of (56) is the same as for an unmagnetized sheath. Moreover, since the $\mathbf{E}\times\mathbf{B}$ drift velocity is much less than the electron thermal velocity, the wall potential is only weakly dependent on the angle of incidence.

Equation (42) is now solved using a standard shooting method, i.e., we choose a value for the electric field at the wall, which in turn fixes the value of the wall potential through (56), and numerically integrate (42) as an initial value problem. If the value of the electric field is chosen incorrectly, the calculated potential will not asymptote to zero as we move into the plasma. Hence we select a new value for the electric field at the wall and iterate until $\Psi(\xi\to\infty)=0$. The results of this technique are shown in Fig. 18 where we have plotted $\ln|\Psi|$ for $\alpha=5$ and $\epsilon=1°$, 5°, and 9°. We note that the wall potential is essentially independent of the angle of incidence, and that the scale length of the sheath decreases for increasing angle of incidence. This change in the scale length is attributable to the filling in of the perpendicular ion distribution function by ions flowing along the field lines. (Recall that in the absence of the ion loss function, i.e., if the ions also have a Boltzmann distribution all the way to the wall, the sheath scales on the Debye length.)

The most notable of the previous works in the regime of oblique incidence is that of Chodura.[5] In addition to his two-fluid analysis of the presheath region, which was referenced earlier in conjunction with the generalized Bohm condition, he used a particle-in-cell code to determine the equilibrium sheath profiles as a function of the angle of incidence of the magnetic field. It is difficult to make a detailed comparison between the two theories, since the majority of his work is done for $\epsilon\geqslant 10°$, a regime where we would expect our analysis to begin to fail due to the strong coupling of the parallel and perpendicular motion. However, in Fig. 19 we compare the results for the case $\alpha=10$, $M/m=100$, and $\epsilon=10°$. It is interesting to note that both techniques produce the same wall potential; however, his results indicate a longer scale length for the sheath potential. We believe that this is due to his use of an insufficient number of particles in the simulation, thereby resulting in an initial potential drop at the edge of the source region of the simulation.

VI. DISCUSSION AND CONCLUSIONS

Our analysis of the sheath formed between a magnetized plasma and a particle absorbing wall for the case in which the magnetic field intercepts the wall with a small angle of incidence, ϵ, shows that in the parameter regime of interest, i.e., $r_{ci}\gg L_D\gg r_{ce}$ and $0°\leqslant\epsilon\leqslant 9°$, there are two distinct regimes of sheath formation: (1) grazing incidence, where $\epsilon\lesssim\nu/\Omega_e$, and (2) oblique incidence, where $\epsilon\gg\nu/\Omega_e$. In the first case, the sheath characteristics are determined by the parameter λ, which measures the ratio of the convective and diffusive electron flows out of the plasma. If $\lambda\lesssim 1$, the wall potential is negative and the sheath scale length is on the order of an ion gyroradius. If $\lambda\gtrsim 1$, the wall potential is positive and the sheath is characterized by two scale lengths: a short-length region adjacent to the wall is followed by a region of the order of the ion gyroradius region in the plasma interior. The value of λ for which the wall potential changes sign is found to be independent of both the temperature ratio, T_e/T_i and the scale-length ratio $k_D r_{ci}\propto n^{1/2}B^{-1}$. For fixed internal parameters (i.e., n, T, and E_y), an increase in ϵ results in a decrease in λ. In the case of oblique incidence, the potential at the wall is negative, with a value close to that of the

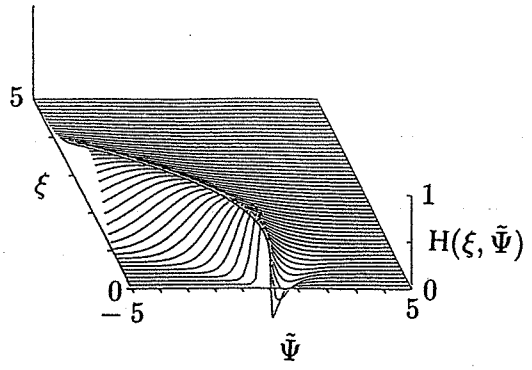

FIG. 20. Plot of the function $H(\xi,\tilde{\Psi})$ for the range $-5\leqslant[\tilde{\Psi}=q(\Phi_w-\Phi)/T_e]\leqslant 5$ and $0\leqslant(\xi=x/r_{ci})\leqslant 5$.

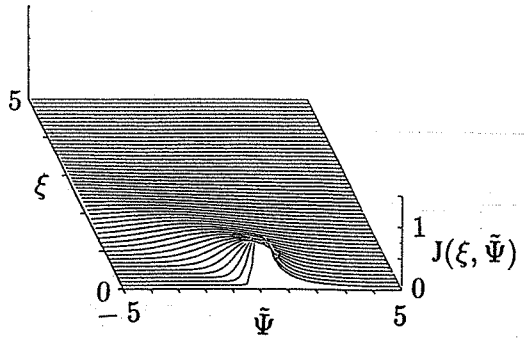

FIG. 21. Plot of the function $J(\xi,\tilde{\Psi})$ for the range $-5\leqslant[\tilde{\Psi}=q(\Phi_w-\Phi)/T_e]\leqslant 5$ and $0\leqslant(\xi=x/r_{ci})\leqslant 5$.

unmagnetized plasma sheath, and the scale length, which is on the order of an ion gyroradius, is a weakly decreasing function of ϵ.

In conclusion, the model we have presented predicts a wide variety of behavior for the magnetized plasma sheath. In the proper limits, we have seen that the results are in good agreement with those of previous models. Moreover, we have been able to extend our analysis into regimes which have not been previously studied. This is particularly true for the case of grazing incidence, where we have been able to observe the transition from positive to negative wall potentials. Since sheaths are found in all laboratory plasmas, it is hoped that the improved understanding of the physical process involved in magnetized sheath formation will be of value to a wide range of researchers.

ACKNOWLEDGMENTS

We wish to thank Dr. M. Gerver and Dr. R. Sydora for their helpful discussions.

This work was supported by the U.S. Department of Energy.

APPENDIX: THE ION LOSS FUNCTION $I(\xi,\tilde{\Psi})$

In Sec. II, we found that the modification of the ion density profile, due to the presence of a particle absorbing wall, is described by the function

$$I(\xi,\tilde{\Psi})=\frac{1}{\sqrt{\pi}}\int_0^\infty du\,\exp[-(u+u_{y0})^2]\operatorname{erf}\sqrt{2\xi u}, \tag{A1}$$

where

$$u_{y0}(\xi)=-\left(\frac{\xi^2+\theta\tilde{\Psi}(\xi)}{2\xi}\right) \tag{A2}$$

and $\tilde{\Psi}(\xi)=\Psi_w-\Psi(\xi)$. This function is plotted in Fig. 3. As can be seen, if $\tilde{\Psi}>0$, the majority of the ions are confined in the plasma, even for distances small compared with the ion cyclotron radius. If $\tilde{\Psi}<0$, on the other hand, the ion population is severely depleted by the wall for distances up to several ion cyclotron radii. In addition, we note that for the range of $\tilde{\Psi}$ plotted, I has reached its asymptotic value (unity) within 5 ion gyroradii.

In Sec. IV, we found that to evaluate the sheath equation, we needed an expression for the derivative of the ion density profile and, hence, an expression for the derivative of I. This is most easily evaluated using the alternative form for I,

$$I(\xi,\tilde{\Psi})=\frac{1}{\sqrt{\pi}}\int_{u_{y0}}^\infty du\,\exp(-u^2)\operatorname{erf}\sqrt{2\xi(u-u_{y0})}. \tag{A3}$$

Differentiating this integral, yields

$$\frac{dI}{d\xi}=\frac{2}{\pi}\int_{u_{y0}}^\infty du\,\frac{\exp[-u^2-2\xi(u-u_{y0})]}{\sqrt{2\xi(u-u_{y0})}}\times\left(u-\frac{d}{d\xi}[(\xi u_{y0})]\right). \tag{A4}$$

If we introduce the shifted variable $s=u-u_{y0}$, this becomes

$$\frac{dI}{d\xi}=\frac{2}{\pi}\int_0^\infty ds\,\frac{\exp[-(s+u_{y0})^2-2\xi s]}{\sqrt{2\xi s}}\times\left(s+u_{y0}-\frac{d}{d\xi}[\xi(u_{y0})]\right). \tag{A5}$$

The derivative in the above equation is evaluated using our expression for u_{y0}, (A2) yielding

$$\frac{d}{d\xi}(\xi u_{y0})=-\xi+\frac{\theta}{2}\frac{d\Psi}{d\xi}. \tag{A6}$$

Substituting this into the equation for $dI/d\xi$, and separating the integral into the parts which depend on $d\Psi/d\xi$, and those that do not, we have

$$\frac{dI}{d\xi}=\frac{1}{\pi\sqrt{\xi}}\exp(-u_{y0}^2)\left\{-\frac{\theta}{\sqrt{2}}\frac{d\Psi}{d\xi}\mathcal{I}\left(\frac{1}{2}\right)+\sqrt{2}\left[\mathcal{I}\left(+\frac{1}{2}\right)+(u_{y0}+\xi)\mathcal{I}\left(-\frac{1}{2}\right)\right]\right\}, \tag{A7}$$

where

$$\mathcal{I}(\pm\tfrac{1}{2})=\int_0^\infty ds\,s^{\pm 1/2}\exp[-s^2-2(u_{y0}+\xi)s]. \tag{A8}$$

Integral (A8) is evaluated using formula 3.462.1 of Gradshteyn and Ryzhik,[9] yielding

$$\varphi(-\tfrac{1}{2})=2^{-1/4}\Gamma(\tfrac{1}{2})\exp[\tfrac{1}{2}(u_{y0}+\xi)^2]\,D_{-1/2}[\sqrt{2}(u_{y0}+\xi)] \tag{A9}$$

and

$$\varphi(+\tfrac{1}{2})=2^{-3/4}\Gamma(\tfrac{3}{2})\exp[\tfrac{1}{2}(u_{y0}+\xi)^2]\,D_{-3/2}[\sqrt{2}(u_{y0}+\xi)], \tag{A10}$$

where $D_\nu(t)$ is the parabolic cylinder function of order ν and argument t. Substituting the results for $\varphi(\pm\frac{1}{2})$ into (A7), and simplifying, we have

$$\frac{dI}{d\xi}=H-\theta J\frac{d\Psi}{d\xi}, \tag{A11}$$

where

$$H=(2^{1/4}/\pi\sqrt{\xi})\exp[-u_{y0}^2+\tfrac{1}{2}(u_{y0}+\xi)^2]$$
$$\times\{[\Gamma(\tfrac{3}{2})/\sqrt{2}]\,D_{-3/2}[\sqrt{2}(u_{y0}+\xi)]$$
$$+\Gamma(\tfrac{1}{2})(u_{y0}+\xi)\,D_{-1/2}[\sqrt{2}(u_{y0}+\xi)]\} \tag{A12}$$

and

$$J=\frac{\Gamma(\frac{1}{2})}{\pi 2^{3/4}\sqrt{\xi}}\exp\left(-u_{y0}^2+\frac{1}{2}(u_{y0}+\xi)^2\right)$$
$$\times D_{-1/2}[\sqrt{2}(u_{y0}+\xi)]. \tag{A13}$$

Surface plots of the functions H and J are given in Figs. 20 and 21, respectively.

[1]U. Daybelge and B. Bein, Phys. Fluids **24**, 1190 (1981).
[2]K. Theilhaber and C. K. Birdsall, Phys. Fluids B **1**, 2244 (1989).
[3]K. Theilhaber and C. K. Birdsall, Phys. Fluids B **1**, 2260 (1989).
[4]M. J. Gerver, S. E. Parker, and K. Theilhaber, Phys. Fluids B **2**, 1069 (1990).
[5]R. Chodura, Phys. Fluids **25**, 1628 (1982).
[6]D. L. Holland, Ph.D. thesis, University of California at Los Angeles, 1990.
[7]S. E. Parker, X. Q. Xu, A. J. Lichtenberg, and C. K. Birdsall, Phys. Rev. A **45**, 3949 (1992).
[8]C. K. Birdsall, IEEE Trans. Plasma Sci. **PS-19**, 65 (1991).
[9]I. S. Gradshteyn and I. M. Ryzhik, *Table of Integrals, Series, and Products* (corrected and enlarged edition), edited by A. Jeffrey (Academic, New York, 1980).